RESEARCH ARTICLE

Synthesis of lignite-based Ni/C composite with low-medium temperature pyrolysis method as an efficient Pt-free counter electrode for dye-sensitized solar cells

Wei Mao[1] · Liguo Wei[1] · Lishuang Zhao[1] · Xiaohu Xu[1] · Jianmin Lin[1] · Huiyi He[1] · Xindan Zhang[1] · Zihan Zhang[1]

Abstract

In order to obtain inexpensive Pt-free counter electrode materials for dye-sensitized solar cells and expand the application fields of low-rank coal, lignite-based Ni/C composite was prepared by low-medium temperature pyrolysis method using Huolinhe lignite as raw materials. The structure and chemical components of as-synthesized lignite-based Ni/C composite was characterized by XRD, FT-IR, TG, Raman, SEM, TEM, and XPS, and the electrocatalytic activity of lignite-based Ni/C composite counter electrode was investigated by cyclic voltammetric curve, electrochemical impedance spectrum, and Tafel polarization curve. It is found that the electrocatalytic activity of the lignite was improved after low-medium temperature pyrolysis and composited with Ni species to form lignite-based Ni/C composite, which helps to catalyze the reduction of electrolyte and thus improve the photoelectric conversion efficiency of the solar cells. The photoelectric conversion efficiency (η) of the dye-sensitized solar cells based on the lignite-based Ni/C composite counter electrode was 3.42% (J_{sc} = 11.49 mA cm^{-2}, V_{oc} = 0.75 V, FF = 0.40) significantly higher than that of the lignite counter electrode (η = 0.20%, J_{sc} = 3.16 mA cm^{-2}, V_{oc} = 0.72 V, FF = 0.09). This indicates that low-medium temperature pyrolysis and composition with Ni are an effective method to improve the photovoltaic performance of lignite-based counter electrode materials.

Graphical abstract

Thelignite-based Ni/C composite was synthesized and applied in counter electrodefor DSSCs.
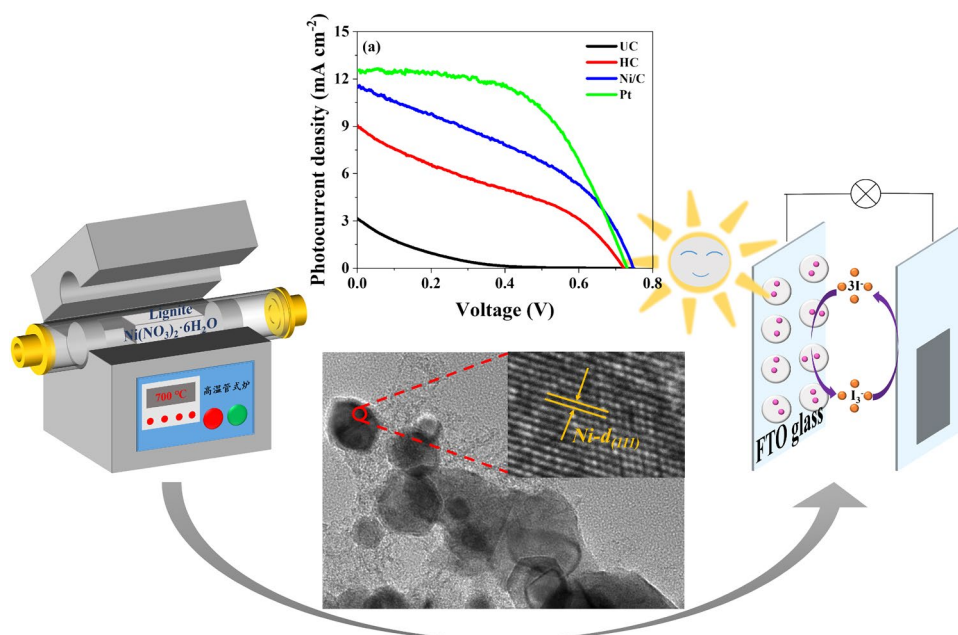
Extended author information available on the last page of the article

1 Introduction

With the development of society and the continuous improvement of living standards for people, the demand for energy is growing and the energy crisis is becoming increasingly serious. Therefore, the vigorous development of new renewable energy is urgent [1]. Solar energy, as an inexhaustible source of energy, has the advantages of non-pollution and cleanliness, and how to efficiently transfer it to electric energy using a valid device is a key issue [2]. Recently, dye-sensitized solar cells (DSSCs) stand out from the crowd of solar cells due to their simple fabrication process, low cost, and promising applications. DSSCs are mainly composed of three main parts: TiO_2 photoanode, electrolyte solution, and counter electrode. Counter electrode plays a crucial role in the reduction of I_3^- to I^- and the transfer of electron from the external circuit to the electrolyte [3–5]. Therefore, the photovoltaic performance of DSSCs could be greatly affected by its counter electrode materials. Pt is considered to be an extremely suitable counter electrode material for catalyzing the triiodide reduction reactions in DSSCs with I_3^-/I^- electrolyte solution [6]. However, the commercialization of DSSCs devices using Pt as counter electrode is limited due to the high price and low reserve quantity of Pt. Therefore, to reduce the cost of DSSCs, it is important to explore effective and alternative Pt-free counter electrode materials [7–11]. Currently, research has focused on metal alloys [12], transition metal carbides/nitrides/oxides/sulfides [13–16], and carbonaceous materials [17–20]. Among them, carbonaceous materials have become a hot research topic due to their high electrical conductivity, superior oxidation resistance, and excellent electrochemical stability [21], and more and more types of carbonaceous counter electrode materials were synthesized via various carbon sources [22, 23]. As a member of the carbon material family, coal has been receiving increased attention to its efficient and clean utilization [24, 25]. Lignite is a low-rank coal with rich reserves, which has a high content of oxygen-containing functional groups as well as a specific network space and pore structure [26, 27]. These excellent properties make it promising for applications in the field of optoelectronic materials and for the preparation of catalysts [28]. However, lignite and its derivatives have been neglected for the application in DSSCs as counter electrode materials because of their insufficient conductivity and electrocatalytic activity. Therefore, how to enhance the conductivity and electrocatalytic activity of lignite and its derivatives is a key point for its application in DSSCs [29].

In recent years, many strategies were put forward to control the composition and structure of lignite for its applications in different fields. For example, Zhu et al. successfully prepared electrode materials for supercapacitors by pyrolytic activation using Shengli lignite as raw material, which led to a significant improvement in its electrochemical performance. At current density of 0.2 A g^{-1}, it exhibited a specific capacitance of 449 F g^{-1} [30]. Zhao et al. prepared coal-based carbon fibers using lignite as raw material by electrospinning and maintained it at 800 °C under Ar atmosphere for 1 h to improve its conductivity and applied it as electrode materials for supercapacitors. Finally, a specific capacitance of 230 F g^{-1} was achieved at a current density of 1 A g^{-1} [31]. These literatures indicate that pyrolysis of coal can change the coal molecular structure and increase its conductivity. More importantly, it is also found that the modification of transition metal Ni can improve the electrocatalytic activity of carbon counter electrode materials for the application of DSSCs [32–34], due to their excellent availability, good stability, low cost, and variable valence.

Therefore, in this study, lignite-based Ni/C composite counter electrode materials were prepared by low-medium temperature pyrolysis method using Huolinhe lignite as the raw material. The structure and chemical components of as-synthesized lignite-based Ni/C composite counter electrode materials were characterized by XRD, FT-IR, TG, Raman, SEM, TEM, and XPS. The electrocatalytic activity of lignite-based Ni/C composite counter electrode for the reduction of I_3^- to I^- were investigated by cyclic voltammetric curve, electrochemical impedance spectrum, and Tafel polarization curve. Finally, the effects of pyrolysis temperature, pyrolysis time, and Ni mass percentage on the photoelectric properties of DSSCs were discussed in detail.

2 Experimental sections

2.1 Materials and chemicals

$Ni(NO_3)_2·6H_2O$ (AR) was obtained from Shantou Xilong Chemical Factory, China; ethyl cellulose (CP), titanium dioxide nanoparticles (Richter, 25 nm), propylene carbonate (99.7%), anhydrous lithium iodide (99%), and iodine (99.8%) were purchased from Aladdin Reagent Co., China; dye N719 was available from Solaronix Co, Switzerland. All reagents were used directly without further purification. The lignite used in this experiment is provided by Huolinhe Coal Mine in Inner Mongolia province of China (average particle size < 200 mesh) and its proximate and ultimate analysis are shown in Table 1.

Table 1 Proximate and ultimate analysis of Huolinhe lignite

Industrial analysis/%				$Q_{net, ad}/$ kJ g^{-1}	Elemental analysis/%				
M_{ad}	A_d	V_{ad}	FC_{ad}		C_{ad}	N_{ad}	H_{ad}	O^*_{ad}	$S_{t, ad}$
14.81	10.71	36.70	37.78	19.28	35.76	0.70	1.38	61.85	0.31

ad air drying base, *d* drying base

*Calculated by difference and subtraction method

2.2 Synthesis of lignite-based Ni/C

Lignite-based Ni/C composite was synthesized by low-medium temperature pyrolysis method. Firstly, 1.0 g of Huolinhe lignite (UC) was weighed and put into an agate mortar, and then 0.0779 g of nickel nitrate hexahydrate was added. After evenly ground, the object was put into a porcelain boat pushed to the central position of a quartz tube to ensure that the material was evenly heated. With the assistance of a vacuum pump, the vacuum was drawn to − 0.1 MPa and filled with N_2 to atmospheric pressure, the vacuum process was repeated twice to ensure that there was no air in the quartz tube. After that, the pyrolysis temperature was increased from 20 to 700 °C at a rate of 10 °C min^{-1} and kept at 700 °C for 1 h. The lignite-based Ni/C composite was obtained after cooled down to room temperature and labeled as Ni/C. For comparison, the pyrolyzed lignite material was also prepared by the same method and labeled as HC.

2.3 Counter electrode preparation

The Ni/C counter electrode was prepared as follows: 0.5 mg of lignite-based Ni/C composite was weighed, added into 1.0 mL of anhydrous ethanol, and ground into a paste, then 4 drops of 5% Nafion solution were added and continuously ground to mixed thoroughly. Then drip 10 μL of this mixture onto FTO conductive glass with a microinjector to form a 1×1 cm^2 film and dried in an oven at 80 °C for 30 min to obtain lignite-based Ni/C composite counter electrode. As a comparison, the UC and HC counter electrodes were also prepared by the same method, while Pt counter electrode was prepared by screen-printing method using H_2PtCl_6 paste.

2.4 Fabrication of DSSCs

The TiO$_2$ photoanode with an effective area of 0.16 cm^2 was prepared by screen-printing method. The preparation process was as follows: firstly, 0.18 g TiO$_2$ nanoparticle, 0.09 g ethyl cellulose, and 0.73 g terpineol were weighed into a 10 mL vial, and an appropriate amount of ethanol was added and stirring for about 1 week to form a paste suitable for screen printing. The screen-printing process was repeated 6 times to form a film of 8–12 μm. Thereafter, it was calcined in a muffle furnace at 500°C for 30 min. Then, the obtained

TiO$_2$ photoanode film was placed in 3 mol L^{-1} dye N719 solution overnight to obtain dye-sensitized TiO$_2$ photoanode. A mixture of 0.5 M LiI, 0.1 M 4-tert-butylpyridine, and 0.05 M I$_2$ and acetonitrile-propenyl carbonate was used as the electrolyte, and the electrolyte was dropped to fulfill the space on the septum between the dye-sensitized TiO$_2$ photoanode and the counter electrode, all of which were assembled into DSSCs with a sandwich-like structure by holding with a clamp.

2.5 Materials characterization

An X-ray powder diffractometer (XRD, D8-Advance, Bruker) with a radiation source of Cu-Kα, an operating voltage of 40 kV, and a current of 40 mA was used to carry out phase analysis. The surface morphology and structure of the Ni/C composite was observed by scanning electron microscopy (SEM, Hitachi, S-4800) and high-resolution transmission electron microscope (HR-TEM, Tecnai G2 F30 S-TWIN, FEI, America). X-ray photoelectron spectroscopy (XPS, Thermo VG, ESCALAB250) with a radiation of Al-Kα was used to carried out elemental composition and chemical states. Fourier transform infrared spectroscopy (FT-IR, Nicolet iS5) was used to determine the functional groups contained in Ni/C composite. Thermogravimetric analyzer (TG, LINSEIS STA PT 1600) was used to determine the thermal stability of Ni/C composite.

2.6 Electrochemical measurements

The electrochemical workstation system (CHI 760E, Chenhua, Shanghai) was used to carry out the electrochemical and photovoltaic properties. Cyclic voltammetry (CV) was performed in a three-electrode system with an Ag/AgCl electrode as the reference electrode, a Pt sheet as the auxiliary electrode, the prepared counter electrode as the working electrode, and an acetonitrile solution of 0.01 M LiI, 0.001 M I$_2$ and 0.1 M LiClO$_4$ as the electrolyte. Electrochemical impedance spectroscopy (EIS) was measured by assembling two identical CEs into a symmetric cell with a frequency range of 0.1 Hz to 100 kHz, a voltage amplitude of 10 mV, and zero bias potential. Tafel polarization curves (Tafel) were likewise obtained by assembling two identical electrodes into a symmetric cell at a scan rate of 10 mV s^{-1}. Photocurrent density-voltage measurements ($J-V$) were

performed under an illumination of 100 mW cm^{-2} provided by a solar simulator (AM 1.5 G). Besides, the incident photon-to-current conversion efficiency (IPCE) was measured on a Newport EQE/IPCE spectral response system.

3 Results and discussion

3.1 Morphology and structure

The XRD patterns of the lignite-based Ni/C composite was shown in Fig. 1a. For comparison, the XRD patterns of UC as well as HC were also plotted in the Fig. 1a. From the XRD patterns of UC, it can be seen that a broaden peak corresponding to the (002) crystal plane of graphite type carbon materials appears at 2θ angle of 25.9°, and diffraction peaks of SiO$_2$ species originating from the components contained in the lignite itself were found at 2θ angles of 20.8°, 26.6°, 50.6°, 59.9°, and 68.2°, respectively. After pyrolysis to form HC, diffraction peaks were found at the same positions as UC, indicating that pyrolysis did not change the phase components and carbon materials frameworks of UC. For Ni/C composite, besides the above peaks, some stronger diffraction peaks were also observed at 2θ angles of 44.5°, 51.8°, and 76.4°, consisting with standard card PDF#87-0712 and corresponding to the (111), (200), and (220) crystallographic planes of Ni, respectively. This indicates that Ni rather than NiO is present in the Ni/C composite. Although NiO should

be formed by the direct decomposition of Ni (NO$_3$)$_2$·6H$_2$O, the decomposed NiO species are further reduced by elemental C to form Ni monomers. Therefore, obvious diffraction peaks of NiO species were not found in the Ni/C composite and the Ni species mainly exist in the form of Ni monomers.

In order to investigate the changes of functional groups in the material, FT-IR was carried out. As seen in Fig. 1b, the functional groups located at 465 cm^{-1}, 798 cm^{-1}, and 912 cm^{-1} in UC were associated with O–Si–O and Si–O–M (metal ions), indicating the presence of quartz or inorganic silicate type substances in the material [35]. The peaks located at 600 and 875 cm^{-1} disappear for HC compared to UC, probably because some –O–M bonds were broken during the low-medium temperature pyrolysis. For Ni/C composite, the functional groups located at 600 and 875 cm^{-1} appeared again due to the introduction of –O–Ni after Ni decoration. The functional group at 537 cm^{-1} was associated with the stretching vibrations of –S–S– and –S–H, and the stretching vibrations of the S=O functional group at 1037 cm^{-1} were also detected [36]. The broadening of the sulfur-containing absorption peaks of HC and Ni/C indicated that the sulfur-containing functional groups are lost as sulfur dioxide during the low-medium temperature pyrolysis. The functional group located at 1087 cm^{-1} was a C–H deformation vibration on the aromatic ring [37]. The functional groups located in the 1168–1612 cm^{-1} region were associated with C=O and C–O stretching vibrations [38]. The sharp decreased in HC and Ni/C oxygenated functional

Fig. 1 a XRD patterns of UC, HC, and Ni/C, b FT-IR spectra of UC, HC, and Ni/C, c TG curves of coal, Ni/C, and Ni(NO$_3$)$_2$·6H$_2$O, d Raman spectra of UC, HC, and Ni/C
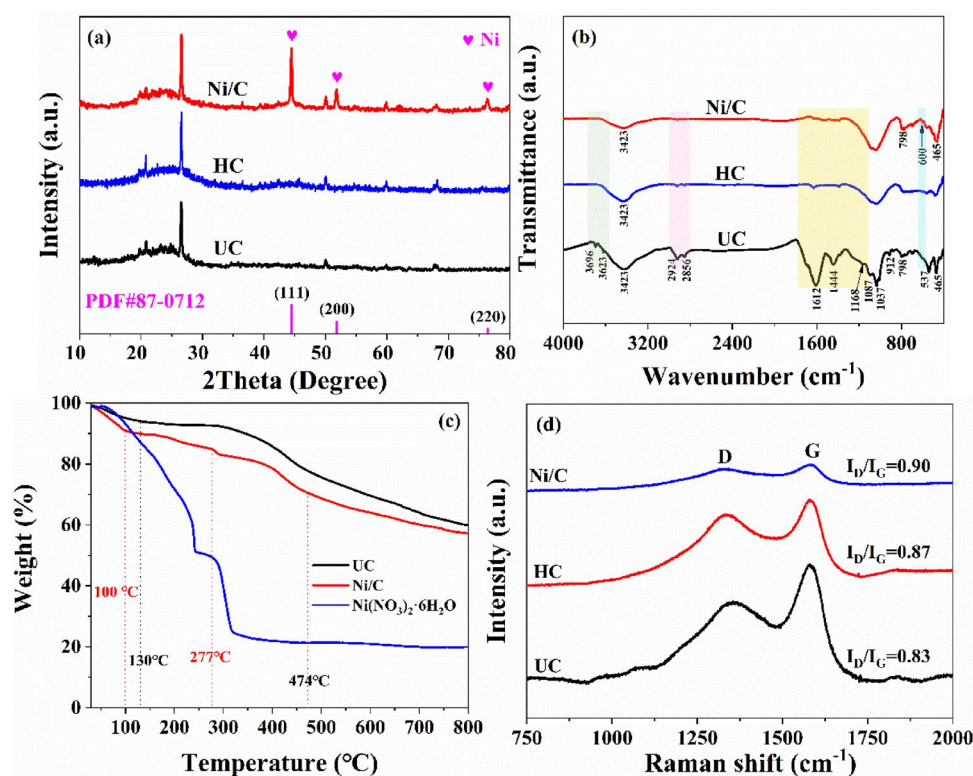
groups in this region was mainly attributed to the loss of carbon dioxide and water during the low-medium temperature pyrolysis and also indicated an increase in graphitization. The functional groups at 2856 and 2924 cm^{-1} were associated with asymmetric $–CH_2–$ and $–CH_3$ stretching vibrations in the lignite [39]. In HC and Ni/C composite, the peak at this position almost disappeared, indicating that $–CH_2–$ and $–CH_3$ were broken during the process of low-medium temperature pyrolysis. The functional group at the peak of 3423 cm^{-1} was associated with the stretching vibration of –OH in the carboxyl group. It can be seen from the Fig. 1b that the absorption peak of UC at 3423 cm^{-1} is the largest, indicating that the UC has the most –COOH. The HC has a broader and less intense –COOH peak compared to UC, indicating that the medium-low temperature pyrolysis can cause some of the –COOH to be lost as carbon dioxide and water. Compared to HC, the –COOH peak of Ni/C composite was also wider and weaker, which is mainly due to the chemical reaction with –COOH after the addition of nickel nitrate hexahydrate, as well as the effect of low-medium temperature pyrolysis. The functional groups located at 3623 and 3969 cm^{-1} could be attributed to the free –OH vibrations in UC [40], which disappeared for HC and Ni/C composite.

In order to monitor the pyrolysis processes of Ni/C composite, TG tests were carried out for the raw materials of UC, $Ni(NO_3)_2·6H_2O$ and Ni/C (namely coal, $Ni(NO_3)_2·6H_2O$, and $coal + Ni(NO_3)_2·6H_2O$). Figure 1c shows that the TG curves of UC, $Ni(NO_3)_2·6H_2O$ and Ni/C composite raw materials measured under N_2 atmosphere. For the UC, the weight decreased by about 8% when the calcination temperature increased to 130°C, corresponding to the loss of H_2O. When the temperature increased from 130 to 474 °C, small organic molecules and aliphatic aromatic hydrocarbon molecules in the materials transformed into water vapor and carbon dioxide, and volatilized in the nitrogen atmosphere with a weight loss of about 24%, which is closely related to the disappearance of peaks located at 1037–1612, 2856, and 2924 cm^{-1} in the FT-IR test. The total weight loss of UC was about 41% from room temperature to 800°C. For the Ni/C composite, the TG curve was very similar to that of UC. However, a different decreasing trend from UC was observed at the beginning of the curve before 100°C, by comparing with the TG curves of $Ni(NO_3)_2·6H_2O$ it is confirmed that this phenomenon was caused by the loss of crystal water in $Ni(NO_3)_2·6H_2O$. When the temperature increased to 277 °C, $Ni(NO_3)_2·6H_2O$ is completely transformed into $Ni(NO_3)_2$ after water loss, which start to pyrolyze to form NiO and accompanied by a certain amount of nitrogen oxide gas emission, so there was a certain weight loss. When the temperature increased to 800°C, the total weight of Ni/C composite decreased by about 43%, which was slightly higher

than that of UC due to the addition of $Ni(NO_3)_2·6H_2O$, and the reduction of NiO to Ni by the C species in the materials.

Figure 1d shows the Raman spectra of UC, HC, and Ni/C. In all three materials, there are two characteristic peaks, one is the D-band at 1346 cm^{-1}, indicating the peak of sp^3-hybridized defect state C, and the other is the G-band at 1593 cm^{-1}, indicating the peak of sp^2-hybridized graphite C. The defects in the material can be determined by the magnitude of the I_D/I_G value, the larger the I_D/I_G value, the more defects in the material, and therefore, the more active sites in the material for I_3^- reduction to I^- [37]. As shown in Fig. 1d, UC has the smallest I_D/I_G value ($I_D/I_G = 0.83$). After low-medium temperature pyrolysis to form HC, the I_D/I_G value becomes larger ($I_D/I_G = 0.87$), indicating that the internal structural defects of the material become more and the catalytic sites increased. Furthermore, The I_D/I_G value of Ni/C increased to 0.90 after simultaneously composited with Ni. Compared to HC, the slightly larger I_D/I_G value of the lignite-based Ni/C composite indicated that the lignite-based Ni/C composite has more defects, which would make Ni/C composite exhibiting a better electrocatalytic activity and further enhanced by the positive effect of Ni doping on the catalytic reduction of I_3^- ions.

In order to observe the microscopic morphology of UC, HC, and Ni/C, SEM for them were carried out and shown in Fig. 2. It can be seen from Fig. 2a that the UC is loosely dispersed, which is not compact enough to ensure the conductivity of the material, indicating worse electrocatalytic activity. However, as shown in Fig. 2b, the HC shows a much compact structure due to some lignite particles coalesces together during the pyrolysis process, and there were still a lot of voids between the compact structures, which are sufficient to ensure electrolyte penetration and efficient electron transfer and resulted in increased electrocatalytic activity. The morphology of the Ni/C composite formed after Ni doping was shown in Fig. 2c–e, respectively. It is found that some small Ni particles are decorated on the surface of lignite, indicating the successfully modified with Ni particles during the pyrolysis process. Therefore, the increased active sites due to Ni decoration and the good conductivity after low-medium temperature pyrolysis ensured the charge transfer and the occurrence of the triiodide/iodide redox reaction, which indicated the high electrocatalytic activity of lignite-based Ni/C composite. To better prove the successful synthesis of Ni/C composites, EDS tests were performed on Fig. 2e, and the results are shown in Fig. 2f (carbon), g (oxygen), and h (nickel). It can be seen from Fig. 2f and g that the carbon and oxygen elements are evenly distributed. Although the distribution of nickel elements is not uniform due to the non-uniform distribution of oxygen-containing functional groups in coal, it again proves that the Ni/C composite was successfully synthesized. The EDS results show
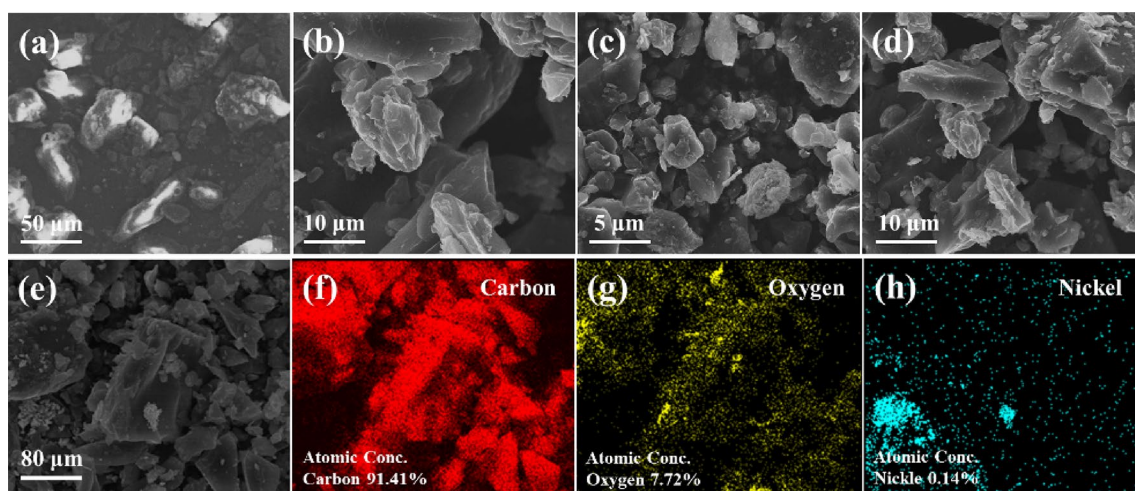
Fig. 2 SEM images of **a** UC, **b** HC, **c–e** Ni/C; EDS elemental mappings of **f** carbon **g** oxygen **h** nickel for Ni/C

that the atomic concentrations of carbon, oxygen, and nickel in the Ni/C material are 91.4, 7.72, and 0.14%, respectively.

Although the atomic concentration ratio of oxygen to nickel is above 1:1, it still did not indicate that the Ni species existed as NiO, but metallic Ni monomers in Ni/C composite. The higher oxygen atomic concentration was partly caused by the formation of some hetero-metal oxide together with very small amount of nickel oxides and some residuals oxygen-containing group or adsorbed oxygen, which was confirmed by the previous XRD test and the same result was obtained in the subsequent XPS test.

Furthermore, the microscopic morphology and structure of Ni/C were observed by transmission electron microscope (TEM). The TEM images of Ni/C composite were shown in Fig. 3a–c. From Fig. 3a–c, it is observed that the Ni monomers were well attached to the lignite surface, which make the lignite-based Ni/C composite have a better electrocatalytic activity. Furthermore, the high-resolution transmission electron microscope (HR-TEM) was performed on the selected local area in Fig. 3c. As shown in the HR-TEM image, a set of lattice fringes was observed. The calculated lattice spacing of the fringes was 2.035 nm, corresponding to the (111) crystal plane of Ni monomer and consisting with the XRD results. The results of HR-TEM further confirmed that the Ni species was mainly existed as Ni monomers in Ni/C composite.

To further demonstrate the successful synthesis of lignite-based Ni/C composites and investigate the elemental composition and their chemical state, XPS tests were performed, and the results were shown in Fig. 4. From the results in Fig. 4a, it can be seen that C 1s and O 1s peaks were present near the binding energy of 284.50 eV and 532.26 eV for both UC, HC and Ni/C composites. In addition, the Ni 2p peak was found at 854.44 eV for the Ni/C composite. To further
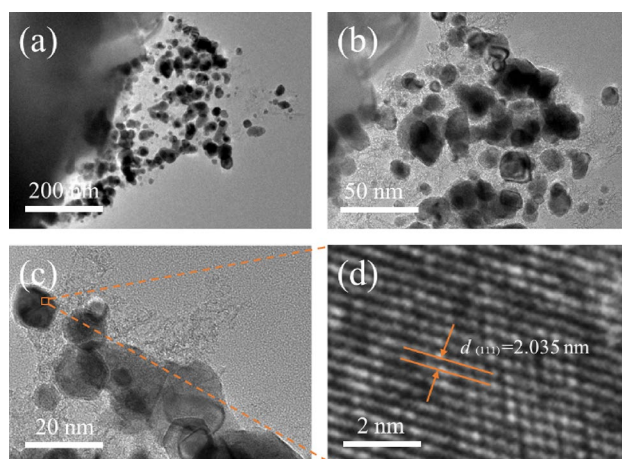

Fig. 3 **a–c** TEM images of Ni/C, **d** HR-TEM image of the framed area in **c**

investigate the effect of low-medium temperature pyrolysis and modification of Ni on the carbon structure of UC, the high resolution C 1s spectra of UC was given in Fig. 4b, and for comparison, the high resolution C 1s spectra of HC and Ni/C composite was also plotted in Fig. 4b. The results showed that three carbon structures existed in all materials, namely C–C/C=C located around 284 eV, C–O located around 285 eV, and C=O located around 288 eV [41]. The peak positions were almost unchanged after low-medium temperature pyrolysis and Ni modification, indicating that the oxygen-containing group was not completely destroyed after low-medium temperature pyrolysis and Ni modification, which was consistent with the FT-IR and EDS analysis. Figure 4c shows the high-resolution fitting spectra of O 1s fits for UC, HC, and Ni/C composites. Vacant oxygen (O^{2-}, 530.9 eV), free oxygen (O^-, 532.2 eV), and adsorbed oxygen

Fig. 4 **a** XPS spectra of UC, HC, and Ni/C, **b** the C 1s spectra of UC, HC, and Ni/C, **c** the O 1s spectra of UC, HC, and Ni/C, **d** the Ni 2p spectra of Ni/C
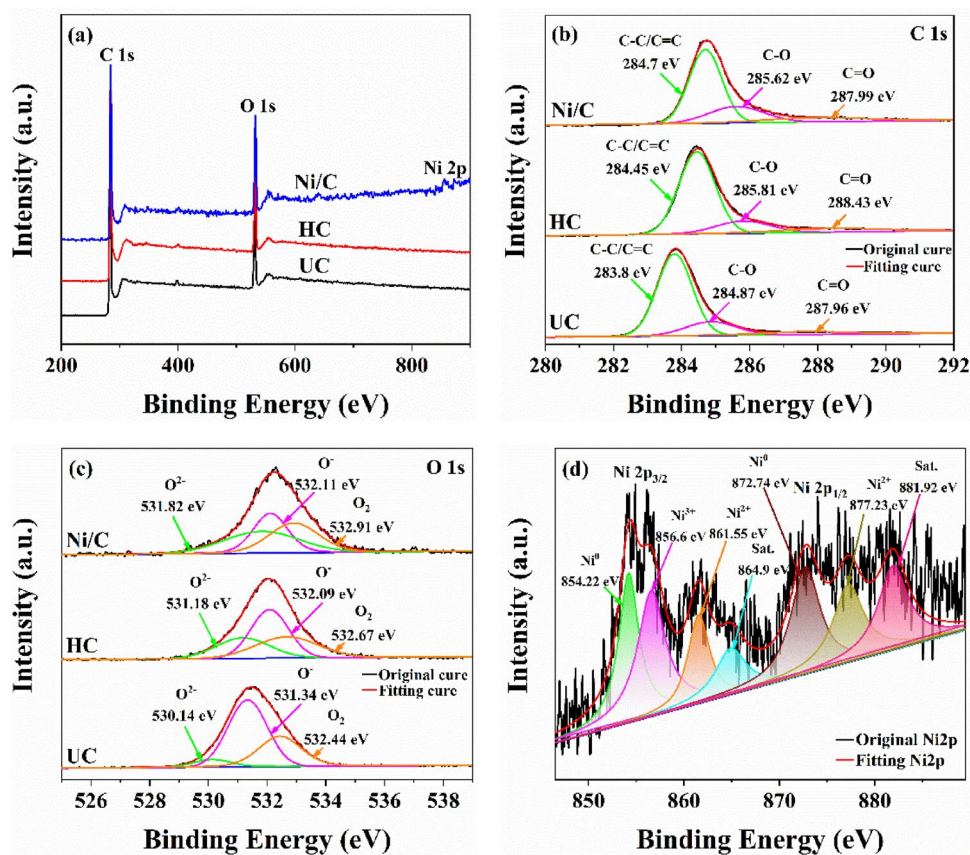

(O_2, 533.12 eV) are present in each material [42]. From the Fig. 4c, it is found that the O^{2-} area in the material becomes larger after the pyrolysis, mainly because there is a small amount of metal oxide formation in the lignite during the pyrolysis process, which makes the O^{2-} content inside the HC become more. After Ni modification, the O^{2-} of the material continued to increase, mainly due to the decomposition of nickel nitrate to produce Ni oxides. Although most of them were reduced to Ni monomers by C, a small amount of Ni_2O_3 was also attached to the Ni surface (the amount of Ni_2O_3 too little to be detected by XRD, but visible in the Ni 2p high-resolution). So, after the modification of Ni, the content of O^{2-} continues to increase, as evidenced by the Ni^{3+} in the Ni 2p high-resolution image in Fig. 4d. Figure 4d showed the high-resolution fit of Ni 2p in the Ni/C composite. It can be seen from the Fig. 4d that two satellite peaks appear at 864.9 eV and 881.92 eV, and the peaks corresponding to Ni $2p_{3/2}$ and Ni $2p_{1/2}$ were located at binding energies of 855.35 eV and 873.1 eV, respectively. In addition, Ni^0 peaks were found at binding energies of 854.22 eV and 872.74 eV, indicating the presence of Ni monomer in the lignite-based Ni/C composite.

Finally, Ni/C composite counter electrodes were prepared by drop-coating method and the corresponding TiO_2 photoanodes were also prepared by a screen-printing method.

Since the surface morphologies and thickness of both counter electrode and working electrode play an important role in the performance of DSSCs, they were carefully investigated by SEM, and shown in Fig. 5. Figure 5a–c is the top view SEM images of UC, HC, and Ni/C counter electrodes, respectively. It is clearly seen from Fig. 5a–c that the materials coated on FTO class does not exhibit a compact film structure due to the uneven particle size. Hence, there is negative effect on the performance of DSSCs. However, it is seen that there are some Ni particles on the material of Ni/C counter electrode in Fig. 5c, which contribute to the conductivity and electrocatalytic activity of the Ni/C counter electrode, thereby contributing to the improvement of photovoltaic performance of DSSCs. From the top view SEM images of TiO_2 photoanode (Fig. 5d), it can be seen that TiO_2 nanoparticles formed a compact film structure on the surface of FTO glass. The cross-section SEM images of UC, HC, and Ni/C counter electrodes (Fig. 5e–g) determined the difference between the lignite with/without pyrolysis and with/without Ni modification. It is clearly seen that the thickness ($l \approx 40$ μm) of UC, HC, and Ni/C counter electrodes was not obviously changed after pyrolysis and Ni modification. From the cross-section SEM images of TiO_2 photoanode (Fig. 5h) it is found that the thickness of the TiO_2 photoanode coated on the FTO glass was about 18 μm.

Fig. 5 **a-c** Top view SEM images of UC, HC and Ni/C counter electrodes **d** Top view SEM images of TiO$_2$ photoanode **e-g** Cross-section SEM images of UC, HC and Ni/C counter electrodes **h** Cross-section SEM images of TiO$_2$ photoanode
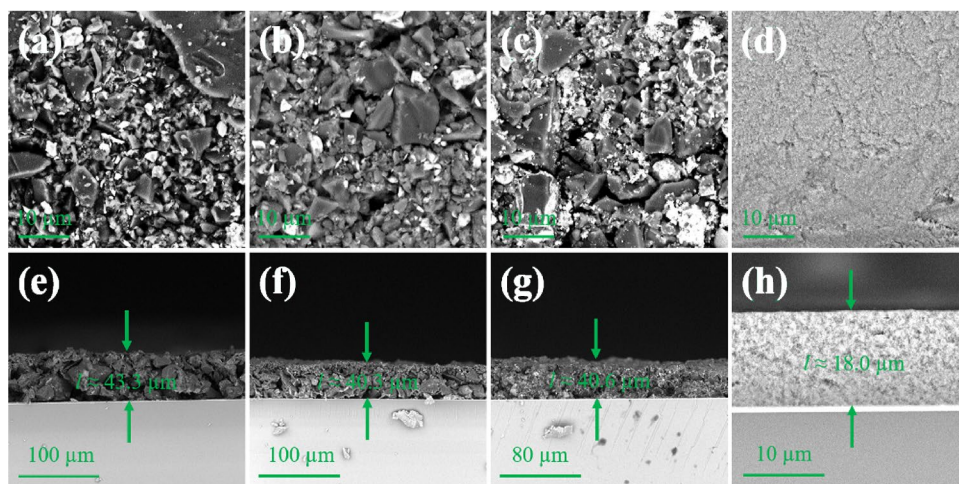
3.2 Electrocatalytic activity and photovoltaic properties

3.2.1 Electrochemical impedance spectroscopy

In order to evaluate the charge transfer dynamics of the Ni/C composite, electrochemical impedance spectroscopy (EIS) was performed using a symmetric cell assembled by two same counter electrodes with a structure of counter electrode-electrolyte-counter electrode, and the Nyquist plots and equivalent circuit of the prepared symmetric cells are shown in Fig. 6a. It can be seen from Fig. 6a that the Nyquist plots of each material consists of a semicircle in the high-frequency region. The intersection of the semicircle in the high-frequency region with the X-axis is the series ohmic resistance (R_s) between the counter electrode film and the FTO conductive glass, and the magnitude of R_s has some influence on the conductivity of the counter electrode [43]. From the enlarged view of the boxed area in Fig. 6a (the inset of Fig. 6a), it is found that R_s (Pt) < R_s (Ni/C) < R_s (UC) < R_s (HC). During the pyrolysis process, the oxygen element in the material of UC reacted with carbon element leading to the reduction of oxygen element content, making the adhesion of HC to the surface of FTO conductive glass becoming poor. However, the R_s of Ni/C composite after Ni modification is greatly reduced, indicating that the doping of Ni can improve the conductivity. The radius of the semicircle in the high frequency area represented the charge transfer resistance (R_{ct}) of the material, which directly reflected the electrocatalytic activity of the material for the triiodide/ iodide redox reaction [44]. It can be seen from Fig. 6a that R_{ct} (Pt) < R_{ct} (Ni/C) < R_{ct} (HC) < R_{ct} (UC). Furthermore, the R_s and R_{ct} values for the electrode materials were fitted using the equivalent circuit shown in the inset of Fig. 6a, and the results are shown in Table 2. From Table 2, the R_s values of the four counter electrode materials (UC, HC, Ni/C, and Pt) were 27.4 Ω, 38.6 Ω, 24.1 Ω, and 22.8 Ω, respectively, and

their R_{ct} values were 728.6 Ω, 17.72 Ω, 7.28 Ω, and 3.45 Ω, respectively. The lower R_{ct} of Ni/C composites proved that the materials had better electrocatalytic activity. The above results indicated that the conductivity of UC was significantly improved after low-medium temperature pyrolysis and modification by Ni, which was benefit for enhancing the photoelectric properties of DSSCs.

3.2.2 Tafel polarization curves

To investigate the electrocatalytic activity of the counter electrodes, Tafel polarization curves of symmetric cells were tested. In general, Tafel polarization curve contained three regions: diffusion region, Tafel region, and polarization region, and two parameters: exchange current density (J_0) and limit diffusion current density (J_{lim}) to evaluate the electrocatalytic activity of the counter electrode [45]. J_0 is the Y-axis reading of the intersection of tangent line to the cathode branch in the Tafel zone and the perpendicular line to the zero potential [46], and J_{lim} is the intersection of the cathode's branch and the Y-axis [47]. In addition, J_0 and J_{lim} can also be calculated from the Eqs. (1) and (2).

$$J_0 = \frac{RT}{nFR_{ct}} \tag{1}$$

$$J_{lim} = \frac{2neDCN_A}{l} \tag{2}$$

In Eq. (1), n, F, T, and R denote the number of electrons transferred by the reaction, Faraday's constant, absolute temperature, and gas constant, respectively. In Eq. (2), n, e, D, C, N_A, and l denote the number of electrons transferred by the reaction, basic charge, diffusion coefficient of triiodide, concentration of I$_3^-$, Avogadro's constant, and thickness of the spacer layer, respectively. As can be seen in Fig. 6b, UC has the smallest J_0 and J_{lim}, indicating that it had the worst

Fig. 6 **a** Nyquist plots curves for symmetric dummy cells fabricated with different counter electrodes (the inset shows an enlarged view of the boxed area and equivalent circuit diagram applicable to fit Nyquist plots). **b** Tafel polarization curves of symmetric dummy cells with different counter electrodes. **c** CV curves of UC, HC, Ni/C, and Pt counter electrodes for triiodide/iodide redox couple. **d** IPCE for DSSCs based on different counter electrodes
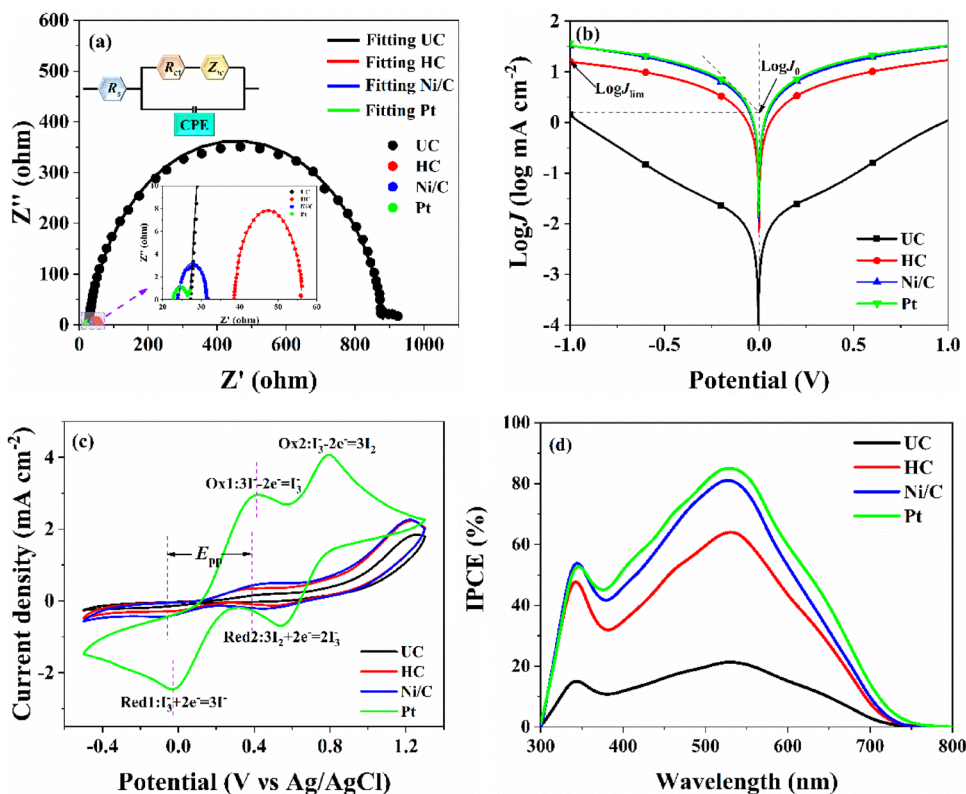
electrocatalytic activity. After low-medium temperature pyrolysis, its electrocatalytic activity was enhanced due to the formation of compact internal structure and the existence of certain interstices and edges in the HC, which helped the occurrence of the triiodide/iodide redox reaction, and thus

UC, HC, Ni/C, and Pt counter electrodes were performed at a scan rate of 10 mV s^{-1} with a three-electrode system. Figure 6c showed the CV curves of different counter electrodes, and it can be clearly observed that each curve had two pairs of redox peaks labeled as Ox1:3I$^-$ − 2e$^-$↔I$_3^-$/Red1:I$_3^-$ +

Table 2 The photovoltaic parameters of different counter electrodes

| Counter electrodes	V_{oc} (V)	J_{sc} (mA cm^{-2})	J_{sc}^{I} (mA cm^{-2})	FF	η (%)	R_{ct} (Ω)	R_s (Ω)
UC	0.72	3.16	3.04	0.09	0.20±0.01	728.6	27.4
HC	0.72	9.06	8.92	0.33	2.14±0.02	17.7	38.6
Ni/C	0.75	11.49	11.14	0.40	3.42±0.01	7.28	24.1
Pt	0.73	12.56	12.37	0.56	5.10±0.03	3.45	22.8

the electrocatalytic ability was enhanced. After the modification with Ni, the electrocatalytic activity of Ni/C composite is further improved and more closed to Pt counter electrode. These confirmed that the electrocatalytic activity of UC was enhanced after low-medium temperature pyrolysis and modification with Ni.

3.2.3 Cyclic voltammetric curves

To further investigate the electrocatalytic activity of the counter electrode for the reduction of I$_3^-$ to I$^-$, CV tests on

2e$^-$↔3I$^-$ and Ox2:I$_3^-$ − 2e$^-$↔3I$_2$/Red2:3I$_2$ + 2e$^-$↔2I$_3^-$, where the electrocatalytic activity is mainly influenced by the first pairs of redox peak [48]. From the first pair of redox peak, the cathode peak current density (J_{pc}) and the peak spacing between Ox1/Red1 (E_{pp}) can be extracted to evaluate the electrocatalytic activity of counter electrode. The smaller the E_{pp} and the larger the J_{pc}, the better the electrocatalytic activity for reduction of triiodide to iodide [49]. As shown in Fig. 6c, the UC counter electrode has the largest E_{pp} and the smallest J_{pc}, indicating that the UC counter electrode has the worst electrocatalytic activity for

Fig. 7 **a** $J-V$ curves of DSSCs with UC, HC, Ni/C, and Pt counter electrodes. **b** Effect of pyrolysis temperature on the photoelectric properties of DSSCs with Ni/C counter electrodes. **c** Effect of pyrolysis time on the photoelectric properties of DSSCs with Ni/C counter electrodes. **d** Effect of Ni mass percentage on the photoelectric properties of DSSCs with different Ni/C counter electrodes
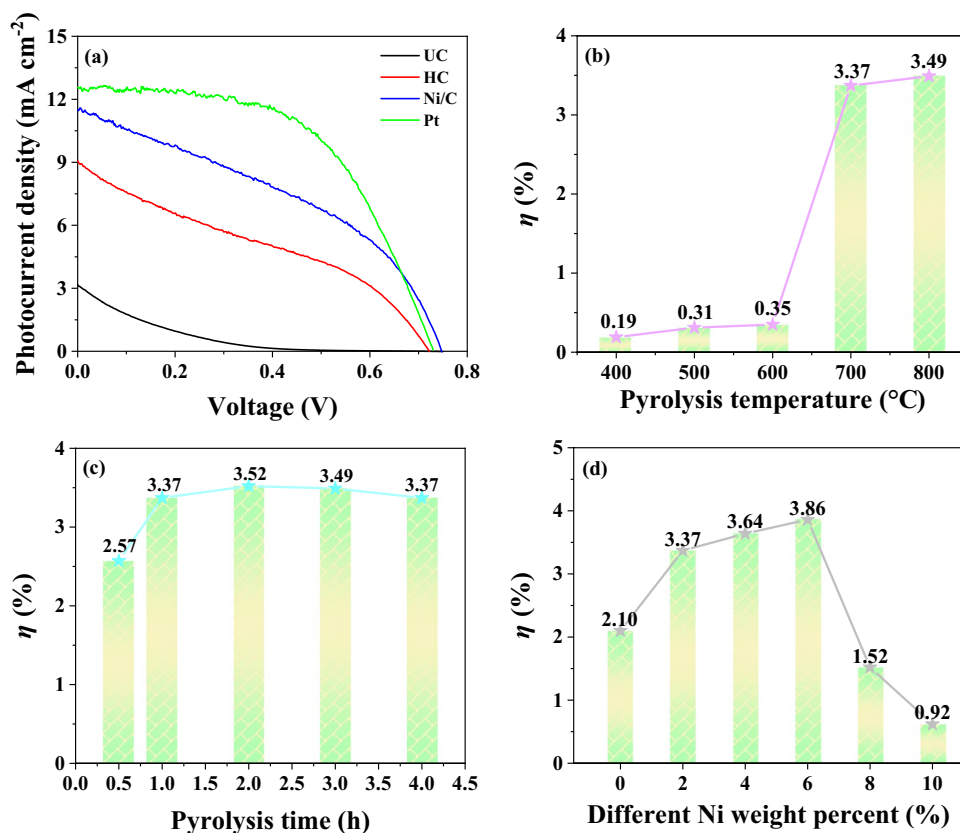
reduction of triiodide to iodide. After the formation of HC by low-medium temperature pyrolysis, E_{pp} decreases and J_{pc} increases, indicating that the electrocatalytic activity of UC is enhanced after low-medium temperature pyrolysis. The Ni/C counter electrode material formed after low-medium temperature pyrolysis and Ni modification has the largest J_{pc} and smaller E_{pp}, indicating that the redox reaction rate is faster on the Ni/C counter electrode, which is more favorable to the occurrence of triiodide/iodide redox reaction, and thus the photoelectric conversion efficiency of DSSCs was improved.

3.2.4 *J–V* Characteristic curves

To investigate the practical application of the lignite-based Ni/C counter electrode, the photovoltaic performance of the DSSCs was tested under simulated solar irradiation (AM 1.5 G, 100 mW cm^{-2}). Table 2 and Fig. 7a show the photovoltaic parameters of different counter electrodes. It can be seen that the DSSCs with Ni/C composite counter electrode exhibited a photovoltaic conversion efficiency ($\eta = 3.42\%$, $V_{oc} = 0.75$ V, $J_{sc} = 11.49$ mA cm^{-2}, $FF = 0.40$), which was significantly better than the UC counter electrode ($\eta = 0.20\%$, $J_{sc} = 3.16$ mA cm^{-2}, $V_{oc} = 0.72$ V, $FF = 0.09$) and HC counter electrode ($\eta = 2.14\%$, $J_{sc} = 9.06$ mA cm^{-2}, $V_{oc} = 0.72$ V, $FF = 0.33$). From the above, it can be seen that

the FF, V_{oc}, and J_{sc} values of the Ni/C composite counter electrode have been improved compared with the UC and HC counter electrodes. The increasement of FF value is mainly due to the decrease of the total resistance of DSSCs based on Ni/C composite counter electrode. The higher V_{oc} is mainly due to the fast electron transport and reduced total resistance of Ni/C counter electrode. Moreover, the Ni/C counter electrode has better electrocatalytic activity, which is beneficial to the reduction of I_3^- to I^-, thus facilitating full regeneration of dye. More importantly, full regeneration of dye increases the electron injection efficiency, thereby increasing the current density of the photo-generated electrons (J_{inj}). Note that the J_{inj} is directly related to the V_{oc} through the Eq. (3)

$$V_{oc} = \frac{KT}{e} \ln \frac{J_{inj}}{qek_{et}c_{ox}N_c} + \frac{E_{ref}}{e} \tag{3}$$

where N_c is the density of states in the TiO$_2$ conduction band, J_{inj} is the current density of photogenerated electrons, q is the number of electrons involved in the charge-transfer process to the oxidized species of concentration c_{ox} with transfer rate k_{et} and elementary charge e, K is the molar gas constant, T is the temperature, and E_{ref} is the difference between the TiO$_2$ conduction band edge (E_c) and the redox potential of the I_3^-/I^- redox coupling electrolyte. According

to the Eq. (3), under the same conditions, the Ni/C counter electrode has better J_{inj} due to its better electrocatalytic activity. Therefore, the Ni/C counter electrode has higher V_{oc} compared to UC and HC counter electrodes [50]. The higher J_{sc} is mainly attributed to the rapid reduction of I_3^- by the counter electrode material due to more I^- would be produced for dyes regeneration, ensuring efficient light capture and a higher photoelectrons injection. To confirm this, the IPCE test were carried out and shown in Fig. 6d. It can be seen from Fig. 6d that the IPCE value of DSSCs based on Ni/C counter electrode enhanced significantly. By comparing these DSSCs devices, it is found that all the component are the same expect the counter electrode. Therefore, the difference is caused by the different of counter electrode. Ni/C counter electrode with higher conductivity and electrocatalytic activity shows enhanced IPCE response due to its rapid reduction of I_3^- and more I^- would be produced for dyes regeneration, ensuring efficient light capture and a higher photoelectrons injection. After calculated from IPCE, the integrated short-circuit current density J_{sc}^I was obtained [51], and listed in Table 2. As seen in Table 2, the J_{sc}^I value obtained from IPCE test are consistence with J_{sc} from $J-V$ test. In view of the above electrocatalytic and electrochemical characterization, due to the increasement in conductivity and electrocatalytic activity by low-medium temperature pyrolysis and modification with Ni, it is suggested that the photoelectric properties of the lignite-based Ni/C composite counter electrode were improved. Although the conductivity and adhesion of Ni/C composite to the FTO conductive glass are not as good as those of Pt, making the photovoltaic performance of the Ni/C composite counter electrode was lower than that of the Pt counter electrode ($\eta = 5.10\%$, $J_{sc} = 12.56$ mA cm^{-2}, $V_{oc} = 0.73$ V, $FF = 0.56$), the synthesis of Ni/C composites by a simple low-medium temperature pyrolysis and Ni modification method substantially improved the electrochemical properties of lignite-based counter electrode, thus greatly improving the photovoltaic performance of DSSCs and becoming a promising counter electrode material to replace Pt.

In order to further investigate the effects of synthesis condition (pyrolysis temperature and time) and modification amount of Ni on the photoelectric properties of lignite-based Ni/C counter electrode, the photoelectric properties of DSSCs with different Ni/C counter electrodes were tested and the results are shown in Fig. 7b–d. From Fig. 7b, it can be found that the photoelectric properties of lignite-based Ni/C counter electrode gradually increased with the increase of pyrolysis temperature. When the pyrolysis temperature is 400 ℃, 500 ℃, and 600 ℃, the photoelectric conversion efficiency is low, which is mainly because the temperature is too low and the internal structure of lignite is not broken enough to form regular molecular structure, resulting in poor conductivity. When the temperature rises to 700 ℃, the internal structure of lignite tends to be regular, so the photoelectric conversion efficiency reaches the best. When the temperature rises to 800°C, the photoelectric conversion efficiency does not change much, which indicates that the structure of Ni/C is similar when the pyrolysis temperature is 700 °C and 800 °C, and the totally pyrolysis is occurred when the temperature reach to 700 °C, which is consistent with TG results. As shown in Fig. 7c, with the increase of pyrolysis time, the photoelectric conversion efficiency of DSSCs with Ni/C counter electrode increased first and then tended to be stable when the pyrolysis time was 1, 2, 3, and 4 h, which means that totally pyrolysis is occurred and Ni has formed a better crystal type during this time range, and there is no obvious difference on the role of redox reaction. Finally, the effect results of Ni mass percentage content on the photoelectric conversion efficiency are shown in Fig. 7d. It can be seen from Fig. 7d that the photoelectric conversion efficiency gradually increases with the increasement of Ni mass percentage content, and reaches to the best when the Ni content is 6%. Although it is said that the modification of Ni can improve the electrocatalytic activity of the material, it will sacrifice the conductivity of the material, so the photoelectric conversion efficiency of the lignite-based Ni/C composite decreases rapidly when the mass percentage content of Ni is more than 6%.

4 Conclusion

In conclusion, lignite-based Ni/C composite counter electrode materials were prepared by low-medium temperature pyrolysis and Ni modification. The low-medium temperature pyrolysis helps to improve the conductivity and electrocatalytic activity of lignite materials, which are further enhanced by Ni modification to form lignite-based Ni/C counter electrode materials. The photoelectric conversion efficiency of DSSCs based on Ni/C counter electrode was 3.42%, which was higher than that of DSSCs based on UC counter electrode (0.20%) and HC counter electrode (2.14%). What's more, the Ni/C composites have the advantages of simple preparation, low cost, and good catalytic activity for I_3^- reduction, which have great potential for replace Pt counter electrode in DSSCs. The exploration of lignite-based Ni/C composite counter electrodes is of significance to broaden the application of lignite and realize its efficient and clean utilization.

Author contributions WM: Most of the experiments and the clutching of the first draft. LW: Language embellishment of the first draft and analysis of experimental data. LZ: Revision of the first draft and layout of the paper. XX: Experimental data processing and image processing. JL: Preparation of materials and assembly of DSSCs. HH: Preparation of materials and assembly of DSSCs. XZ: Analysis of XRD test data and graphing. ZZ: Analysis of XRD test data and graphing.

Declarations

Conflict of interest There are no issues to declare.

References

1. O´Regan B, Grätzel M (1991) A low-cost, high-efficiency solar cell based on dye-sensitized colloidal TiO_2 films. Nature 353(6346):737–740. https://doi.org/10.1038/353737a0

2. Marchini E, Caramori S, Bignozzi CA, Carli S (2021) On the use of PEDOT as a catalytic counter electrode material in dye-sensitized solar cells. Appl Sci 11(9):3795. https://doi.org/10.3390/app11093795

3. Dao VD, Larina LL, Jung KD, Lee JK, Choi HS (2014) Graphene-NiO nanohybrid prepared by dry plasma reduction as a low-cost counter electrode material for dye-sensitized solar cells. Nanoscale 6(1):477–482. https://doi.org/10.1039/c3nr04871c

4. Bae KH, Dao VD, Choi HS (2017) Utility of Pt in PtNi alloy counter electrodes as a new avenue for cost effective and highly efficient liquid junction photovoltaic devices. J Colloid Interface Sci 495:78–83. https://doi.org/10.1016/j.jcis.2017.01.118

5. Sun D, Wang W, Liang B, Xu J, Hu XH, Yang Q, Zuo XQ, Li G, Jin SW (2021) Enhanced electrocatalytic activity in dye-sensitized solar cells via interface coupling of the $CoFe_2O_4/Co_3Fe_7$ heterostructure. J Electroanal Chem 899:115676. https://doi.org/10.1016/j.jelechem.2021.115676

6. Pang B, Zhang M, Zhou C, Dong HZ, Ma S, Feng JG, Chen YJ, Yu LY, Dong LF (2021) Heterogeneous $FeNi_3/NiFe_2O_4$ nanoparticles with modified graphene as electrocatalysts for high performance dye-sensitized solar cells. Chem Eng J 405:126944. https://doi.org/10.1016/j.cej.2020.126944

7. Hagfeldt A, Grätzel M (2000) Molecular photovoltaics. Acc Chem Res 33(5):269–277. https://doi.org/10.1021/ar980112j

8. Park E, Lee Y, Dao VD, Cam NTD, Choi HS (2017) Design of CoNi alloy/graphene as an efficient Pt-free counter electrode in liquid junction photovoltaic devices. Synth Met 230:97–104. https://doi.org/10.1016/j.synthmet.2017.06.002

9. Sim E, Dao VD, Choi HS (2018) Pt-free counter electrode based on FeNi alloy/reduced graphene oxide in liquid junction photovoltaic devices. J Alloys Compd 742:334–341. https://doi.org/10.1016/j.jallcom.2018.01.278

10. Gullace S, Nastasi F, Puntoriero F, Trusso S, Calogero G (2020) A platinum-free nanostructured gold counter electrode for DSSCs prepared by pulsed laser ablation. Appl Surf Sci 506:144690. https://doi.org/10.1016/j.apsusc.2019.144690

11. Dao VD, Larina LL, Tran QC, Bui VT, Nguyen VT, Pham TD, Mohamed IMA, Barakat NAM, Huy BT, Choi HS (2017) Evaluation of Pt-based alloy/graphene nanohybrid electrocatalysts for triiodide reduction in photovoltaics. Carbon 116:294–302. https://doi.org/10.1016/j.carbon.2017.02.004

12. Kamarulzaman UA, Rahman M, Suait MS, Umar AA (2021) Nickel palladium alloy-reduced graphene oxide as counter electrode for dye-sensitized solar cells. J Mol Liq 326:115289. https://doi.org/10.1016/j.molliq.2021.115289

13. Wu CX, Li R, Wang YL, Lu S, Lin J, Liu YC, Zhang XT (2020) Strong metal-support interactions enable highly transparent Pt-Mo_2C counter electrodes of bifacial dye-sensitized solar cells. Chem Commun 56(69):10046–10049. https://doi.org/10.1039/d0cc03744c

14. Jiang QW, Li GR, Liu S, Gao XP (2010) Surface-nitrided nickel with bifunctional structure as low-cost counter electrode for dye-sensitized solar cells. J Phys Chem C 114(31):13397–13401. https://doi.org/10.1021/jp1035184

15. Kakroo S, Surana K, Bhattacharya B (2020) Electrodeposited MnO_2-NiO composites as a Pt free counter electrode for dye-sensitized solar cells. J Electron Mater 49(3):2197–2202. https://doi.org/10.1007/s11664-019-07925-w

16. Li LD, Zhang XY, Fu YH, Han X, Wang Y, Zhang YC, Zhang WM (2021) $NiCo_2S_4$ nanotube arrays grown in situ on Ni foam as a low-cost counter electrode for dye-sensitized solar cells. Sol Energy 225:297–304. https://doi.org/10.1016/j.solener.2021.07.048

17. Kim JH, Hong SK, Yoo SJL, Woo CY, Choi JW, Lee D, Kang JW, Lee HW, Song M (2020) Pt-free, cost-effective and efficient counter electrode with carbon nanotube yarn for solid-state fiber dye-sensitized solar cells. Dyes Pigm 185:108855. https://doi.org/10.1016/j.dyepig.2020.108855

18. Yu HY, Qian C, Ren HJ, Chen M, Tang DM, Wu HY, Lv RG (2020) Enhanced catalytic properties of bimetallic sulfides with the assistance of graphene oxide for accelerating triiodide reduction in dye-sensitized solar cells. Sol Energy 207:1037–1044. https://doi.org/10.1016/j.solener.2020.07.047

19. Hui W, Yun HH (2012) Graphene as a counter electrode material for dye-sensitized solar cells. Energy Environ Sci 5(8):8182–8188. https://doi.org/10.1039/c2ee21905k

20. Costa RD, Feihl S, Kahnt A, Gambhir S, Officer DL, Wallace GG, Lucio MI, Herrero MA, Vzquez E, Syrgiannis Z, Prato M, Guldi DM (2013) Carbon nanohorns as integrative materials for efficient dye-sensitized solar cells. Adv Mater 25(45):6513–6518. https://doi.org/10.1002/adma.201301527

21. Kouhnavard M, Ludin NA, Ghaffari BV, Sopian K, Ikeda S (2015) Carbonaceous materials and their advances as a counter electrode in dye-sensitized solar cells: challenges and prospects. ChemSusChem 8(9):1510–1533. https://doi.org/10.1002/cssc.201500004

22. Kumarasinghe KDMSPK, Kumara GRA, Rajapakse RMG, Liyanage DN, Tennakone K (2019) Activated coconut shell charcoal based counter electrode for dye-sensitized solar cells. Org Electron 71:93–97. https://doi.org/10.1016/j.orgel.2019.05.009

23. Ahmed ASA, Xiang WC, Abdelmotalleib M, Zhao XJ (2022) Efficient NiO impregnated walnut shell-derived carbon for dye-sensitized solar cells. ACS Appl Electro Mater 4(3):1063–1071. https://doi.org/10.1021/acsaelm.1c01216

24. Li YJ, Wang GL, Wei T, Fan ZJ, Yan P (2016) Nitrogen and sulfur co-doped porous carbon nanosheets derived from willow catkin for supercapacitors. Nano Energy 19:165–175. https://doi.org/10.1016/j.nanoen.2015.10.038

25. Muraoka M, Tominaga H, Nagai M (2012) Iron addition to vietnam anthracite coal and its nitrogen doping as a PEFC non-platinum cathode catalyst. Fuel 102:359–365. https://doi.org/10.1016/j.fuel.2012.05.029

26. Jing HY, Shi YT, Song XD, Liang SX, Wu DY, An YL, Hao C (2019) Dual sites of CoO nanoparticles and Co-N_x embedded within coal-based support toward advanced triiodide reduction. ACS Sustain Chem Eng 7(12):10484–10492. https://doi.org/10.1021/acssuschemeng.9b00938

27. Wang CL, Meng FN, Wang TH, Ma TL, Qiu JH (2014) Monolithic coal-based carbon counter electrodes for highly efficient dye-sensitized solar cells. Carbon 67:465–474. https://doi.org/10.1016/j.carbon.2013.10.019

28. Jing HY, Shi YT, Qiu WW, Wu DD, Song XD, An YL, Hao C (2019) Onion-like graphitic carbon covering metallic nanocrystals derived from brown coal as a stable and efficient counter electrode for dye-sensitized solar cells. J Power Sources 414:495–501. https://doi.org/10.1016/j.jpowsour.2019.01.042

29. Chen M, Shao LL (2016) Review on the recent progress of carbon counter electrodes for dye-sensitized solar cells. Chem Eng J 304:629–645. https://doi.org/10.1016/j.cej.2016.07.001

30. Zhu SQ, Chen QL, Shi YY, Chen ZY, Bao RQ, Zhou L, Hou LR, Hui KN, Yuan CZ (2016) Lignite-derived mesoporous N- and O-enriched carbon sheet: a low-cost promising electrode for high-performance electrochemical capacitors. J Solid State Electrochem 20(3):713–723. https://doi.org/10.1007/s10008-015-3100-8

31. Zhao HY, Wang LX, Jia DZ, Xia W, Li J, Guo ZP (2014) Coal based activated carbon nanofibers prepared by electrospinning. J Mater Chem A 2(24):9338–9344. https://doi.org/10.1039/c4ta00069b

32. Wei LG, Mao W, Yu FR, Su T, Chen J, He HY, Zou MY, Wang SJ, Lin JM (2021) Solid-state synthesis of Ni decorated needle coke as low-cost Pt-free counter electrode for efficient dye-sensitized solar cells. ChemistrySelect 6(26):6781–6787. https://doi.org/10.1002/slct.202102035

33. Chen X, Liu J, Qian K, Wang JH (2018) Ternary composites of Ni-polyaniline-graphene as counter electrodes for dye-sensitized solar cells. RSC Adv 8(20):10948–10953. https://doi.org/10.1039/c8ra00934a

34. Zheng L, Bao C, Lei SJ, Wang JL, Li FX, Sun PP, Huang N, Fang L, Sun XH (2018) In situ growing CNTs encapsulating nickel compounds on Ni foils with ethanol flame method as superior counter electrodes of dye-sensitized solar cells. Carbon 133:423–434. https://doi.org/10.1016/j.carbon.2018.03.062

35. Cetinkaya S, Yurum Y (2000) Oxidative pyrolysis of Turkish lignites in air up to 500°C. Fuel Process Technol 67(3):177–189. https://doi.org/10.1016/S0378-3820(00)00105-3

36. Ibarra J, Moliner R, Bonet AJ (1994) FT-IR investigation on char formation during the early stages of coal pyrolysis. Fuel 73(6):918–924. https://doi.org/10.1016/0016-2361(94)90287-9

37. Akhter MS, Keifer JR, Chughtai AR, Smith DM (1985) The absorption band at 1590 cm^{-1} in the infrared spectrum of carbons. Carbon 23(5):589–591. https://doi.org/10.1016/0008-6223(85)90096-X

38. Giroux L, Charland JP, Macphee JA (2006) Application of thermogravimetric Fourier transform infrared spectroscopy (TG-FTIR) to the analysis of oxygen functional groups in coal. Energy Fuels 20(5):1988–1996. https://doi.org/10.1021/ef0600917

39. Lin XC, Wang CH, Ideta K, Miyawaki J, Nishiyama Y, Wang YG, Yoon S, Mochida I (2014) Insights into the functional group transformation of a chinese brown coal during slow pyrolysis by combining various experiments. Fuel 118:257–264. https://doi.org/10.1016/j.fuel.2013.10.081

40. Suh WH, Kang JK, Suh YH, Tirrell M, Suslick KS, Stucky GD (2011) Porous carbon produced in air: physicochemical properties and stem cell engineering. Adv Mater 23(20):2332–2338. https://doi.org/10.1002/adma.201003606

41. Xing MY, Shen F, Qiu BC, Zhang JL (2014) Highly-dispersed boron-doped graphene nanosheets loaded with TiO$_2$ nanoparticles for enhancing CO$_2$ photoreduction. Sci Rep 4:6341. https://doi.org/10.1038/srep06341

42. Liu X, Liu W, Ko M, Park M, Kim MG, Oh P, Chae S, Park S, Casimir A, Wu G, Cho J (2015) Metal (Ni, Co)-metal oxides/graphene nanocomposites as multifunctional electrocatalysts. Adv Funct Mater 25(36):5799–5808. https://doi.org/10.1002/adfm.201502217

43. Baptayev B, Mustazheb D, Abilova Z, Balanay MP (2020) Nanostructured flower-shaped CuCo$_2$S$_4$ as a Pt-free counter electrode for dye-sensitized solar cells. Chem Commun 56:12190–12193. https://doi.org/10.1039/D0CC04211K

44. Wang Q, Moser JE, Grätzel M (2005) Electrochemical impedance spectroscopic analysis of dye-sensitized solar cells. J Phys Chem B 109(31):14945–14953. https://doi.org/10.1021/jp052768h

45. Vijaya S, Landi G, Wu JJ, Anandan S (2020) Ni$_3$S$_4$/CoS$_2$ mixed-phase nanocomposite as counter electrode for Pt-free dye-sensitized solar cells. J Power Sources 478:229068. https://doi.org/10.1016/j.jpowsour.2020.229068

46. Lu S, Chen MZ, Wang YL, Li R, Lin J, Zhang XT (2021) Highly efficient MoS$_2$/rGO electrocatalysts for triiodide reduction as Pt-free counter electrode for dye-sensitized solar cells. Sol Energy 220:788–795. https://doi.org/10.1016/j.solener.2021.03.086

47. Liu HY, Qian X, Niu YD, Chen M, Xu C, Wong KY (2020) Hierarchical Ni-MoSe$_x$@CoSe$_2$ core-shell nanosphere as highly active bifunctional catalyst for efficient dye-sensitized solar cell and alkaline hydrogen evolution. Chem Eng J 383:123129. https://doi.org/10.1016/j.cej.2019.123129

48. Boschloo G, Hagfeldt A (2009) Characteristics of the iodide/triiodide redox mediator in dye-sensitized solar cells. Acc Chem Res 42(11):1819–1826. https://doi.org/10.1021/ar900138m

49. Wang MK, Anghel AM, Marsan B, Ha NLC, Pootrakulchote N, Zakeeruddin SM, Grätzel M (2009) CoS supersedes Pt as efficient electrocatalyst for triiodide reduction in dye-sensitized solar cells. J Am Chem Soc 131(44):15976. https://doi.org/10.1021/ja905970y

50. Dao VD, Kim SH, Choi HS, Kim JH, Park HO, Lee JK (2011) Efficiency enhancement of dye-sensitized solar cell using Pt hollow sphere counter electrode. J Phys Chem C 115:25529–25534. https://doi.org/10.1021/jp208295b

51. Dao VD (2017) Comment on "Energy storage via polyvinylidene fluoride dielectric on the counter electrode of dye-sensitized solar cells" by Jiang. J Power Sources 337:125–129. https://doi.org/10.1016/j.jpowsour.2016.10.100

Authors and Affiliations

Wei Mao[1] · Liguo Wei[1] · Lishuang Zhao[1] · Xiaohu Xu[1] · Jianmin Lin[1] · Huiyi He[1] · Xindan Zhang[1] · Zihan Zhang[1]

✉ Liguo Wei
  xiaole6407@sina.com

[1] College of Environmental and Chemical Engineering,
  Heilongjiang University of Science and Technology,
  Harbin 150022, People's Republic of China